

Electronic and atomic structure of the boron-vacancy complex in silicon

M. Sprenger,* R. van Kemp, E. G. Sieverts, and C. A. J. Ammerlaan

Natuurkundig Laboratorium der Universiteit van Amsterdam, Valckenierstraat 65, 1018 XE Amsterdam, The Netherlands

(Received 19 June 1986)

In electron-irradiated boron-doped silicon the electron paramagnetic resonance spectrum Si-G10 has been studied. Earlier this spectrum had tentatively been identified with a boron-vacancy complex in a next-nearest-neighbor configuration. With electron-nuclear double resonance the hyperfine and quadrupole interactions with ^{10}B (nuclear spin $I=3$) and ^{11}B ($I=\frac{3}{2}$) could be determined, and thus the presence of boron be proved. These experimental results turned out to be consistent with the original microscopic model proposed by Watkins. Because of the low triclinic symmetry of the defect, no symmetry-related neighbor sites exist. As a result every neighbor position with a ^{29}Si nucleus gives rise to a distinct hyperfine tensor. Therefore, hyperfine interactions with only eight neighboring ^{29}Si nuclei have been determined. These hyperfine data showed that the distant boron atom causes only a small deviation from mirror-plane symmetry. This observation made it possible to assign six of the hyperfine interaction tensors to specific lattice sites. From the observed hyperfine interactions it was deduced that this neutral BV^0 complex is rather a B^+V^- structure. This model is further supported by the interpretation of the boron quadrupole interaction.

I. INTRODUCTION

In the past much experimental information has been gathered about vacancy-related defects in monocrystalline silicon. As the vacancy is mobile at room temperature, all irradiation experiments, unless performed under low-temperature conditions, yield complexes in which one or more vacancies and/or impurities are involved. Among these defects are vacancy clusters such as divacancies, trivacancies, tetravacancies and even pentavacancies, as well as vacancies paired with impurity atoms. Especially electron paramagnetic resonance (EPR) experiments have been an important tool for the identification of the various defects and for the determination of their atomic and electronic structure. A review of all defects that are identified in EPR has recently been published.¹ An important class of vacancy-related defects is formed by the com-

plexes of vacancies with substitutional impurities, as they comprise the intentionally introduced doping impurities in silicon. The most important features of the various substitutional-impurity vacancy pairs that have been identified with EPR and electron-nuclear double-resonance (ENDOR) techniques are summarized in Table I. The impurities are from the third, fourth, and fifth row of the periodic system. Striking differences exist between these nine centers. In fact, only the phosphorus-, arsenic-, and antimony-vacancy pairs show common features. Especially the EPR spectrum Si-G10, tentatively ascribed to a boron-vacancy pair by Watkins,² takes a somewhat special position. Most peculiar is its low triclinic symmetry. In silicon this has only been observed for two other cases: an iron-related irradiation defect, Si-NL23,¹² and a hydrogen-implantation defect, Si-AA2.¹³

Generally vacancy-impurity pairs are formed both after

TABLE I. Summary of identified substitutional-impurity vacancy complexes in silicon. Electron spin and point-group symmetry are given, as well as the localization of the unpaired electron on the impurity atom and on the nearest silicon atoms, together with their number.

| Complex | Spectrum | Spin | Symmetry | LCAO | LCAO ^{29}Si | | Ref. |
|----------------|----------|---------------|----------|----------|-----------------------|-----|-------|
| | | | | impurity | η^2 (%) | n | |
| BV^0 | G10 | $\frac{1}{2}$ | 1 | $\ll 1$ | 55 | 1 | 2,3 |
| AlV^- | G9 | 1 | $3m$ | 2 | 11 | 3 | 4 |
| GeV^+ | G26 | $\frac{1}{2}$ | m | | | | 5,6 |
| GeV^- | G27 | $\frac{1}{2}$ | m | | | | 5,6 |
| SnV^0 | G29 | 1 | $3m$ | 1 | 12 | 6 | 7 |
| PV^0 | G8 | $\frac{1}{2}$ | m | 1 | 59 | 1 | 8 |
| AsV^0 | G23 | $\frac{1}{2}$ | m | 1 | 59 | 1 | 9 |
| SbV^0 | G24 | $\frac{1}{2}$ | m | 4 | 57 | 1 | 9 |
| PVP^+ | NL1 | $\frac{1}{2}$ | $2mm$ | 0.2 | 29 | 2 | 10,11 |

anneal of low-temperature electron-irradiated samples and after room-temperature irradiation. By low-temperature electron irradiation vacancies are formed. At temperatures in the range 160–180 K vacancies in *p*-type silicon become mobile. Upon such annealing of irradiated aluminum-doped silicon an EPR spectrum, Si-G9, with trigonal symmetry and stable to 200–250°C, was observed. It was convincingly identified as arising from a vacancy and an aluminum atom at nearest-neighbor sites.⁴ Under similar conditions in boron-doped silicon, spectrum Si-G10 arises. As the corresponding defect has a lower annealing temperature of $\sim 0^\circ\text{C}$, this spectrum is not observed after room-temperature irradiation, in contrast to Si-G9. Due to the absence of resolved hyperfine splitting in the EPR spectra, Watkins was not able to confirm the presence of boron in the center. Despite this absence of boron-hyperfine structure, the lower annealing temperature, and the symmetry lower than Si-G9, Watkins concluded that the spectrum arises from a boron-vacancy pair. The microscopic model which he constructed is given in Fig. 1. It shows the boron atom not on the usual nearest-neighbor position of the vacancy, but on a next-nearest-neighbor site. The present study was undertaken in order to exploit the high resolution of the ENDOR technique for the observation of the boron-hyperfine and quadrupole interactions.³ Furthermore, hyperfine parameters from ^{29}Si nuclei, are expected to give information on the microscopic structure of the defect. This microscopic structure is even more interesting because of the low symmetry of the defect.

Recently, in two deep-level transient-spectroscopy (DLTS) studies, several hole traps have been ascribed to a boron-vacancy complex.^{14,15} From both experiments it is concluded that BV is a configurationally bistable defect, i.e., a defect with two different stable configurations, depending on the charge state, which can reversibly be

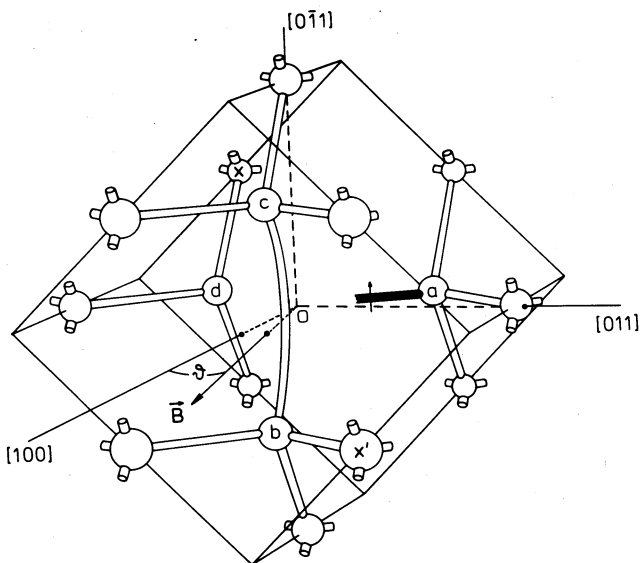


FIG. 1. Model of the boron-vacancy complex, according to Watkins (Ref. 2). The boron atom, marked *x*, is at the lattice position $[\bar{2}\bar{2}0]$, a next-nearest-neighbor position of the vacancy. The electron spin is concentrated mainly at the atom *a*. The orientation is *dba*.

transformed into each other. In ultrafast-quenched boron-doped silicon, Chantre observed two inversely correlated DLTS peaks.¹⁴ He ascribed them to a next-nearest-neighbor configuration, stable as BV^0 , and a nearest-neighbor configuration, stable as BV^+ . After anneal of low-temperature electron-irradiated boron-doped samples, Bains and Banbury ascribed two DLTS peaks to a next-nearest-neighbor, and one to a nearest-neighbor, configuration.¹⁵ Unfortunately, the energies as given in these studies cannot directly be compared, but the published DLTS spectra make it improbable that the same DLTS peaks are discussed. Besides this, some questions remain in connection with EPR experiments: (i) Although Si-G10 anneals at $\sim 0^\circ\text{C}$, Chantre observed only partial transformation at that temperature. (ii) Nearest-neighbor BV^+ , which is probably stable at room temperature, is not EPR active, but why has this configuration never been observed in its metastable paramagnetic BV^0 state? (iii) Reversibility as in DLTS has never been observed in EPR. The present results do not answer these questions. Further experiments are needed to clarify whether, for instance, the last two points are related to the fact that in EPR samples charge carriers are commonly generated by light and not in a selective manner as in DLTS. Yet, bistability, as such, seems an attractive explanation for the occurrence of the present exceptional structure.

In Sec. II the present experiment will be described. Section III gives the hyperfine and quadrupole data of the boron atom and hyperfine data for eight shells of silicon atoms. In Sec. IV these data are discussed in connection with the atomic model.

II. EXPERIMENTS

Our procedure for the production of BV is very similar to that followed by Watkins. It is based upon the knowledge of damage production mechanisms during low-temperature electron irradiation of silicon. In the first stage, immobile vacancies are produced by electron radiation below 20 K. Only in *p*-type material the net vacancy production is high. As silicon self-interstitials are highly mobile under irradiation conditions, even at 4 K, they recombine with vacancies unless they are captured. Watkins showed^{4,16,17} that substitutional acceptor elements form effective traps for self-interstitials, becoming interstitial impurities themselves. After anneal at 160–180 K, mobile vacancies in B-doped material give rise to the spectrum Si-G10.

In a cryostat for combined low-temperature electron-irradiation and spin-resonance measurements, described in detail in Ref. 18, samples of boron-doped float-zone silicon (resistivity $0.1 \Omega \text{ cm}$, $5 \times 10^{17} \text{ B cm}^{-3}$) were irradiated with 1.5 MeV electrons to a fluence of $\sim 10^{17}$ electrons cm^{-2} . During these irradiations the temperature was kept below 18 K. The experimental setup was the same as that used for a similar experiment on the vacancy.^{18,19}

The production of vacancies was monitored by the vacancy-associated EPR spectra Si-G1 and Si-G2. Subsequently, the EPR spectrum Si-G10 was produced by anneal to 190 K for 15 min. Figure 2(a) shows the EPR

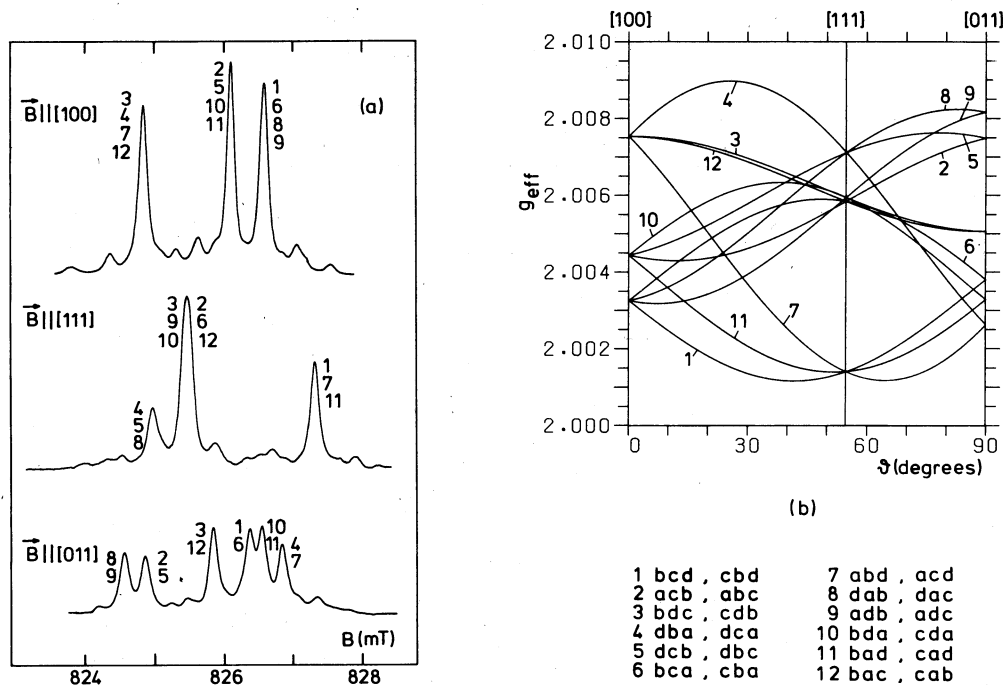


FIG. 2. EPR of the Si-G10 spectrum: (a) EPR spectra with the magnetic field in the three high-symmetry directions of the crystal at a temperature of 18 K and with a microwave frequency of 23.176 GHz. Also visible are the hyperfine satellites of the Si-2 to Si-8 hyperfine interactions. The Si-1 satellites are outside the range of the picture. (b) angular dependence of the effective g values as calculated from a least-squares fit for magnetic field directions in the $(0\bar{1}1)$ plane. The 24 different defect orientations coincide in pairs because the magnetic field is in this plane. The orientation labeling according to Watkins (Ref. 2) is indicated.

spectrum for the three high-symmetry directions of the silicon lattice. In a computer fit of these EPR spectra to the spin Hamiltonian $\mathcal{H} = \mu_B \vec{B} \cdot \vec{g} \cdot \vec{S}$ the six independent elements of the g tensor were determined. In this low symmetry there are no restrictions on the principal axes. The g values in Table II are in close agreement with Watkins's values.² Figure 2(b) shows the angular dependence of the effective g values, for magnetic field directions in the $(0\bar{1}1)$ plane.

ENDOR measurements were performed at a temperature of 18 K in dispersion mode under similar conditions as for V^- .^{18,19} Parameters were determined by a computer fit of the observed ENDOR frequencies to transitions between eigenstates of the Hamiltonian matrices. Due to the low triclinic symmetry of the center, the lattice sites of the ^{29}Si atoms cannot be divided into symmetry classes,

nor can shells of symmetry-related sites exist. Thus, each atom gives rise to a distinct hyperfine interaction tensor of triclinic symmetry.

III. EXPERIMENTAL RESULTS

A. Interactions with the boron atom

In the EPR spectra of Fig. 2(a) no trace of hyperfine interactions with the magnetic boron nuclei is found. Apparently, this splitting is too small to be observed in EPR. In ENDOR experiments, however, the resolving power is three orders of magnitude larger than in EPR, because spectroscopically ENDOR is an NMR experiment. Figure 3 gives examples of ENDOR spectra from the

TABLE II. Electronic g values and boron hyperfine (\vec{A}) and quadrupole (\vec{Q}) interactions of the boron-vacancy complex. Given are principal values (X_i) and principal directions. γ_i is the angle of the i th principal direction with the $(0\bar{1}1)$ plane; δ_i is the angle between the projection of this direction on the $(0\bar{1}1)$ plane and the $[100]$ direction. Hyperfine and quadrupole parameters are in units of kHz, the error is ± 0.5 kHz. The error in the g values is ± 0.0002 . Data refer to orientation dba . The sign of the \vec{A} tensors is chosen such that $\text{tr}(\vec{A}) > 0$. The sign of the \vec{Q} tensors is coupled to that of the \vec{A} tensors.

| \vec{X} | Nucleus | X_1 | X_2 | X_3 | γ_1 | δ_1 | γ_2 | δ_2 | γ_3 | δ_3 |
|-----------|-----------------|--------|--------|--------|------------|------------|------------|------------|------------|------------|
| \vec{g} | | 2.0011 | 2.0051 | 2.0090 | -7.4 | -64.8 | 81.4 | -33.2 | -4.5 | 25.8 |
| \vec{A} | ^{10}B | 183.5 | 154.3 | -180.1 | 53.8 | 72.9 | 21.9 | -50.4 | -27.3 | 27.6 |
| \vec{A} | ^{11}B | 540.8 | 458.8 | -536.6 | 53.7 | 72.6 | 22.1 | -50.9 | -27.2 | 27.0 |
| \vec{Q} | ^{10}B | 25.9 | 10.8 | -36.7 | 36.1 | -32.4 | -51.8 | -54.2 | -10.7 | 49.7 |
| \vec{Q} | ^{11}B | 62.2 | 25.8 | -88.1 | 36.1 | -32.5 | -51.9 | -54.2 | -10.7 | 49.6 |

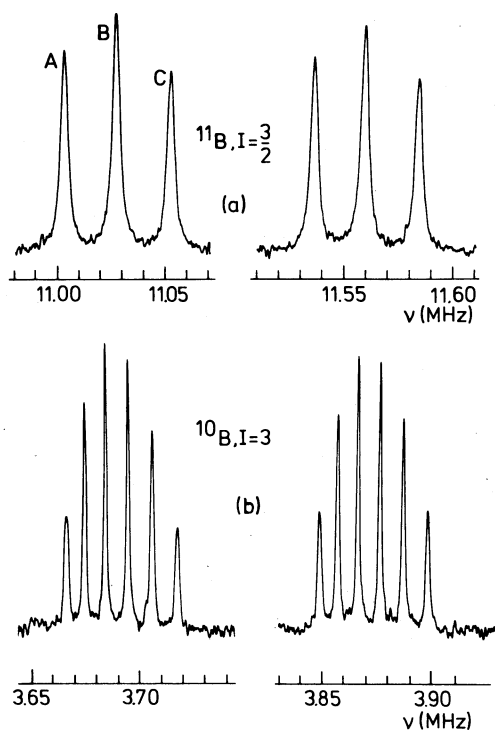


FIG. 3. ENDOR spectra due to boron in the Si-G10 center, from the highest-field EPR line in the [100] direction, $B = 826.73$ mT. (a) ^{11}B , $I = \frac{3}{2}$; (b) ^{10}B , $I = 3$. The differences in intensity are due to different transition probabilities.

highest-field EPR line in the [100] direction [$B = 826.73$ mT, see Fig. 2(a)]. These ENDOR spectra can be understood as arising from the ^{11}B and ^{10}B nuclei, respectively. The ENDOR measurements must be described with a more complicated spin Hamiltonian, comprising the boron nuclear spin,

$$\mathcal{H} = \mu_B \mathbf{B} \cdot \mathbf{g} \cdot \mathbf{S} - g_N \mu_N \mathbf{B} \cdot \mathbf{I} + \mathbf{S} \cdot \vec{A} \cdot \mathbf{I} + \mathbf{I} \cdot \vec{Q} \cdot \mathbf{I}, \quad (1)$$

where \mathbf{S} is the electron spin ($S = \frac{1}{2}$) and \mathbf{I} is the nuclear spin ($I = 3$, ^{10}B , natural abundance 18.8% or $I = \frac{3}{2}$, ^{11}B , 81.2%). These terms represent the electronic Zeeman interaction, the isotropic nuclear Zeeman interaction, the hyperfine interaction between the electronic and nuclear spins, and finally the nuclear quadrupole interaction. The hyperfine interaction tensor \vec{A} has six independent elements in this symmetry, the quadrupole interaction tensor, \vec{Q} , which is taken as traceless, has five. Thus the total spin Hamiltonian of Eq. (1) contains 18 independent parameters for each of the two possible nuclear spin values. The dimension of the matrices is 14×14 in the case of ^{10}B and 8×8 in the case of ^{11}B . First-order energy levels are given by

$$E = g_{\text{eff}} \mu_B B m_S - g_N \mu_N B m_I + A_{\text{eff}} m_S m_I + Q_{\text{eff}} m_I^2. \quad (2)$$

EPR transitions are those with $\Delta m_S = \pm 1$, $\Delta m_I = 0$; NMR transitions (induced in ENDOR) are those with $\Delta m_I = \pm 1$, $\Delta m_S = 0$. The hyperfine splitting in EPR is too small, compared to the EPR linewidth, to be resolved. The ENDOR lines, however, are well separated, as shown

in Fig. 3. For both isotopes two groups of lines are visible, with six and three lines, respectively, each. The two groups lie symmetrically around the nuclear Zeeman frequency $\nu_z = g_N \mu_N B / h$. The splitting A_{eff} between the two groups is due to the hyperfine interaction; the splitting within the groups is due to the quadrupole interaction, $2Q_{\text{eff}}$. For $B \approx 827$ mT the ^{10}B lines are found near 3.78 MHz, the ^{10}B nuclear Zeeman frequency, and the ^{11}B lines near 11.3 MHz. Thus, the two isotopes can be treated separately in the analysis. In the high-symmetry directions slow scans were taken to obtain data points for a least-squares fit. From the angular dependence it was deduced which data points belong to which of the 12 possible orientations. Parameters were obtained in a least-squares program which fits the transitions to the eigenvalues of the Hamiltonian matrices. As ENDOR transitions are, to first order, independent of the electronic g values, these parameters were kept fixed to the values from the EPR fit. Table II gives the principal values and principal directions of the resulting interaction tensors. The nuclear g values (g_N) were determined as 0.6002 ± 0.0001 for ^{10}B and 1.7921 ± 0.0002 for ^{11}B , in close agreement with values found in nuclear tables.²⁰

Because the hyperfine splitting is not resolved in EPR, it is not obvious to which EPR transitions a certain NMR transition is coupled by ENDOR, leaving ambiguity in the sign of the quadrupole interaction with respect to the hyperfine interaction. By a special extension to the ENDOR technique, called field-swept ENDOR (FSE), this ambiguity can be removed.²¹ FSE is a method of obtaining an image of the specific EPR line that is responsible for a certain ENDOR line. In this way (partially) overlapping EPR lines from different orientations, transi-

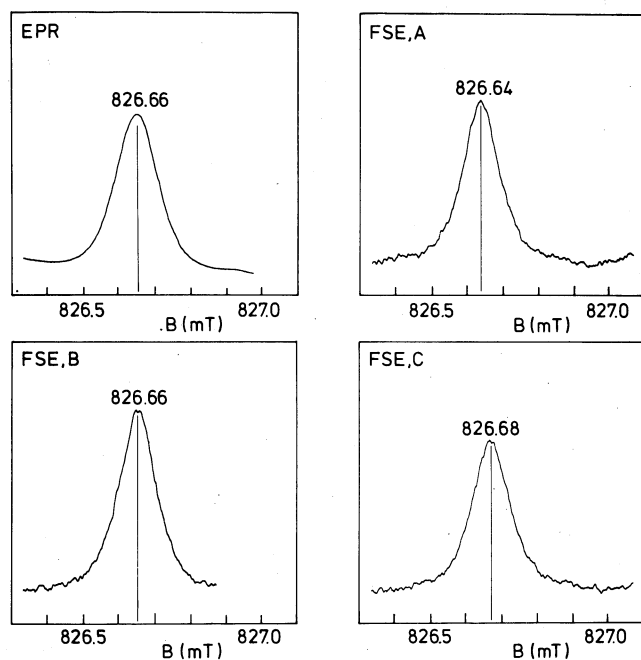


FIG. 4. Field-swept ENDOR (FSE) spectra for $\mathbf{B} \parallel [100]$ of the ^{11}B ENDOR lines A, B, and C of Fig. 3. Also shown is the EPR spectrum, a superposition of all four EPR transitions. Each FSE spectrum is a superposition of only two EPR transitions.

tions, or even defects can be separated. The procedure is to scan the magnetic field, but to monitor the ENDOR signal. If we fix the rf frequency to the required ENDOR transition, a signal is only observed when the magnetic field scan passes a pertinent EPR component. In order to remain on the transition, a small correction has to be applied to the rf frequency as a compensation for the change in nuclear Zeeman frequency due to the field scan. Figure 4 gives FSE spectra in the ^{11}B case, obtained with the three low-frequency ENDOR lines of Fig. 3. Also shown is the total EPR line. Each FSE line is a superposition of only two of the four possible EPR transitions, those which are directly connected to the ENDOR transition. If the FSE lines are at sufficiently different magnetic fields, one can determine which ENDOR transition belongs to which EPR transition(s) and thus determine the sign of the quadrupole interaction tensor with respect to the hyperfine interaction tensor. The separation of the four EPR transitions is given, to first order, by $\Delta B = A_{\text{eff}}/g_{\text{eff}}\mu_B$. For the angle and orientation of the FSE spectra of Fig. 4, $A_{\text{eff}} = 533$ kHz. Thus the expected splitting of the EPR transitions is $\Delta B \approx 18 \mu\text{T}$, which is unresolved under the total EPR linewidth of $120 \mu\text{T}$, but is just resolved as different line positions in FSE. The relative signs of \vec{A} and \vec{Q} in Table II were determined in this way. The angular dependence of the hyperfine interaction A_{eff} and the quadrupole interaction Q_{eff} for the ^{11}B isotope are shown in Fig. 5.

B. Hyperfine interactions with silicon atoms

For the description of the hyperfine interactions of the defect electron ($S = \frac{1}{2}$) with each of the surrounding ^{29}Si atoms ($I = \frac{1}{2}$, 4.7% abundance) we use the spin Hamiltonian

$$\mathcal{H} = \mu_B \mathbf{B} \cdot \vec{g} \cdot \vec{S} - g_N \mu_N \mathbf{B} \cdot \mathbf{I} + \mathbf{S} \cdot \vec{A} \cdot \mathbf{I}. \quad (3)$$

Due to the low symmetry of the defect (point group 1), the hyperfine shells contain only one atom and all hyperfine tensors have this low triclinic symmetry. The intensity of the first-neighbor hyperfine interaction, which is resolved in EPR, is consistent with this number of atoms. The next hyperfine interactions are only partially resolved in EPR, as seen in Fig. 2(a). With ENDOR many more

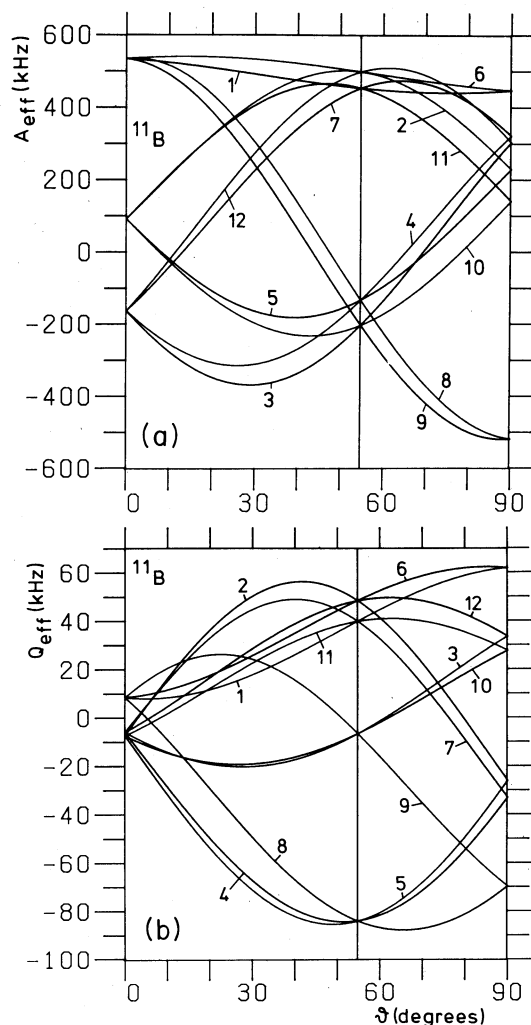


FIG. 5. Angular dependent patterns of (a) hyperfine and (b) quadrupole interactions of the boron-vacancy complex with the ^{11}B nucleus. The magnetic field is in the $(0\bar{1}1)$ plane. Units are kHz. The 24 orientations, which coincide in pairs for fields in the $(0\bar{1}1)$ plane, are numbered 1–12 and their labels are indicated according to Watkins's labeling scheme (Ref. 2).

silicon hyperfine interactions could be resolved, using the procedure as described in the preceding section. Since in the higher-frequency regions the various hyperfine tensors have only little overlap, it was easy to sort out which ENDOR transitions belonged to the same tensor, without

TABLE III. Hyperfine interactions of the boron-vacancy complex with surrounding ^{29}Si atoms. Given are principal values and principal directions as in Table II. Data refer to orientation *dba*. The values of tensor Si-1 are obtained by fitting the EPR data; the others are the result of ENDOR measurements. Units are kHz. ENDOR linewidth was typically 25 kHz. Estimated errors: Si-1, ± 200 kHz; the others, ± 2 kHz.

| Tensor | A_1 | A_2 | A_3 | γ_1 | δ_1 | γ_2 | δ_2 | γ_3 | δ_3 |
|--------|---------|---------|---------|------------|------------|------------|------------|------------|------------|
| Si-1 | 393 900 | 249 900 | 247 800 | -1.9 | -52.6 | 80.6 | 25.9 | -9.2 | 37.7 |
| Si-2 | 67 207 | 56 803 | 55 234 | 49.8 | -4.3 | -36.9 | 22.6 | -13.5 | -77.8 |
| Si-3 | 63 124 | 53 438 | 51 877 | -51.7 | -3.7 | 34.8 | 24.8 | 14.1 | -75.2 |
| Si-4 | 36 125 | 23 624 | 23 049 | -0.6 | -54.0 | 26.6 | 35.7 | -63.4 | 37.1 |
| Si-5 | 35 334 | 22 193 | 21 682 | 0.3 | -54.1 | -27.8 | 35.8 | 62.2 | 36.4 |
| Si-6 | 32 538 | 22 301 | 21 957 | -2.0 | -51.9 | 14.6 | 37.6 | -75.3 | 45.7 |
| Si-7 | 31 708 | 21 632 | 21 270 | 2.7 | -50.6 | -19.5 | 38.4 | 70.3 | 46.9 |
| Si-8 | 32 229 | 20 127 | 19 785 | -0.3 | -53.1 | 89.7 | -55.6 | 0.0 | 36.9 |

making complete angular scans. The nuclear g value was kept constant during the computer fits to the value $g_N = -1.1097$; the electronic g values were kept constant to the values given in Table II. Thus, fits to the six independent elements of the ^{29}Si hyperfine tensors were made. Table III gives the experimental results for the observed tensors. Due to a poor signal-to-noise ratio at high frequencies, we were not able to observe the largest hyperfine tensor in ENDOR for all high-symmetry points. Therefore, the best EPR fit has been used for tensor Si-1. In ENDOR seven more hyperfine tensors were resolved, named Si-2 to Si-8. The next largest hyperfine tensors lie in a frequency region much closer to the ^{29}Si Zeeman frequency at ~ 7 MHz, where the mutual overlap between the hyperfine tensors makes the analysis difficult. Because each lattice site contributes a distinct hyperfine tensor in this symmetry, the number of tensors is large and thus the patterns become obscured by mutual overlap already at higher frequencies than, for instance, for the vacancy.^{18,19} As a consequence of the low symmetry, the eight hyperfine tensors of Table III arise from only eight lattice sites. All of the observed silicon hyperfine tensors are nearly $\langle 111 \rangle$ axial; some angular dependent patterns are given in Fig. 6.

Hyperfine tensors can be decomposed into an isotropic and a traceless part:

$$\vec{A} = a\vec{1} + \vec{B}. \quad (4)$$

The isotropic part is the Fermi-contact interaction which is proportional to the density of the electronic wave function at the site r_0 of the nucleus:

$$a = \frac{2}{3}\mu_0 g\mu_B g_N \mu_N |\Psi(r_0)|^2, \quad (5)$$

where Ψ is the electronic wave function. The anisotropic tensor \vec{B} describes the classical dipole-dipole interaction and can be written

$$B_{ij} = \frac{\mu_0}{4\pi} g\mu_B g_N \mu_N \left\langle \Psi \left| \frac{3x_i x_j}{r^5} - \frac{\delta_{ij}}{r^3} \right| \Psi \right\rangle, \quad (6)$$

where $x_i, x_j = x, y, z$.

The electronic wave function of a defect in silicon is often described as a linear combination of atomic orbitals (LCAO). A one-electron wave function is then written as

$$\Psi = \sum_i \eta_i \phi_i, \quad (7)$$

where i enumerates lattice sites and the contributions ϕ_i on these lattices sites are hybrid combinations of silicon $3s$ and $3p$ orbitals:

$$\phi_i(\mathbf{r}) = \alpha_i \psi_s(\mathbf{r}) + \beta_i \psi_p(\mathbf{r}). \quad (8)$$

Substitution in Eqs. (5) and (6) gives for the Fermi-contact interaction

$$a_i = \frac{2}{3}\mu_0 g\mu_B g_N \mu_N \eta_i^2 \alpha_i^2 |\psi_s(0)|^2, \quad (9)$$

under the assumption that ψ_s and ψ_p decrease sufficiently fast with distance, that at site i only orbitals centered on atom i itself contribute appreciably. Under the same assumption, the anisotropic interaction gives an axial hyper-

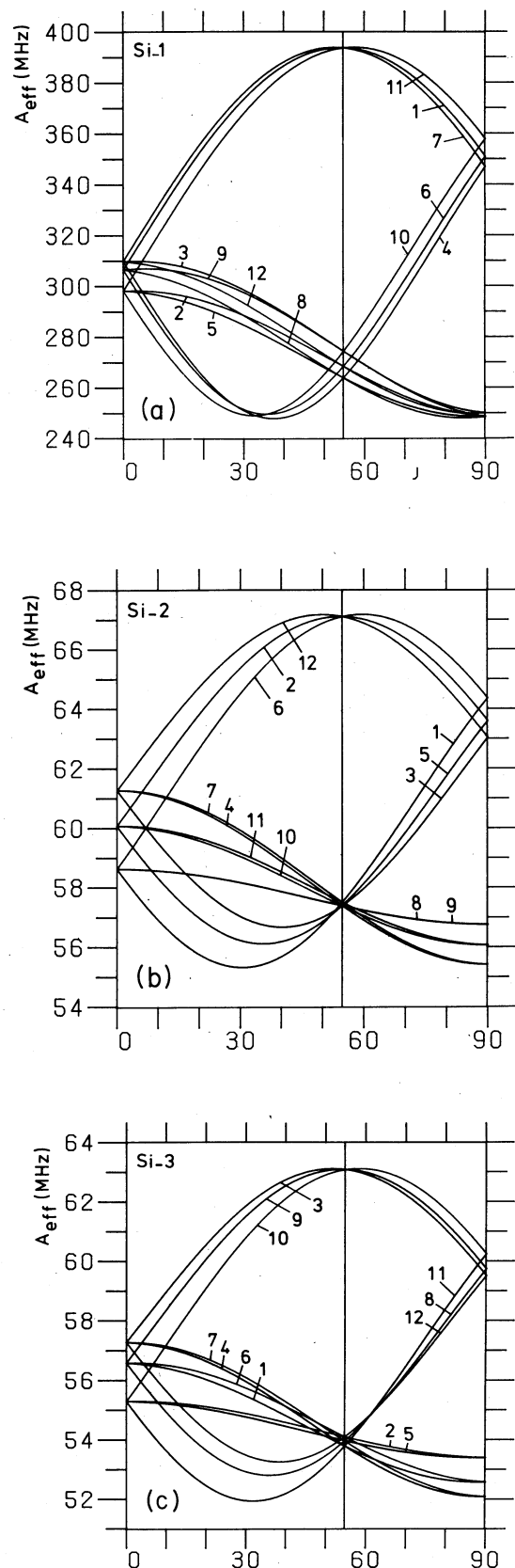


FIG. 6. Angular dependent patterns of hyperfine interactions with ^{29}Si nuclei. (Units are MHz; further presentation as in Fig. 5). Shown are the (a) Si-1, (b) Si-2, and (c) Si-3 interactions. There is a clear resemblance between the pair Si-2 and Si-3 which constitutes a pseudo-G-class shell.

fine tensor \vec{B}_i with principal values $(2b_i, -b_i, -b_i)$, whose axial direction is that of the p lobe and where

$$b_i = \frac{\mu_0}{4\pi} g\mu_B g_N \mu_N \eta_i^2 \beta_i^2 \langle r^{-3} \rangle_p. \quad (10)$$

The quantities $|\psi_s(0)|^2$ and $\langle r^{-3} \rangle_p = \langle \psi_p | r^{-3} | \psi_p \rangle$ are constants from the atomic wave functions and independent of the specific defect.

The experimentally observed hyperfine interactions are not always exactly axially symmetric. In that case, principal values can be equated to $a + 2b$, $a - b + c$, and $a - b - c$, where a is the isotropic part, b is the parameter determining the axially symmetric part, and c is the deviation from axial symmetry. These reduced parameters are given in Table IV. When using for silicon, the values $|\psi_s(0)|^2 = 34.6 \times 10^{30} \text{ m}^{-3}$ and $\langle r^{-3} \rangle_p = 18.2 \times 10^{30} \text{ m}^{-3}$ (Ref. 22), and with $\alpha^2 + \beta^2 = 1$, Eqs. (9) and (10) give the s character fraction α^2 , the p character fraction β^2 , and the degree of localization η^2 , of the paramagnetic electron on the various atomic states. These values are also included in Table IV. The largest fraction of the paramagnetic electron is concentrated on the nearest neighbor (54.83%); the other seven atomic sites contribute 4–5% each. The total localization on the first eight shells is 87.27%.

IV. DISCUSSION

A. Defect structure: silicon hyperfine tensors

In this section we will review Watkins's atomic model² and discuss the implications of our experimental results. A defect with triclinic symmetry, as inferred from the angular dependence in Fig. 2, can have 48 distinct orientations in the silicon lattice. Due to inversion invariance of EPR, at most 24 distinct lines can occur. Moreover, when the magnetic field is in the $(0\bar{1}1)$ crystal plane, resonances coincide pairwise, so that only 12 lines result. Watkins derived a labeling scheme where every orientation label is constructed as a combination of three letters. The letters a , b , c , and d refer to the $\langle 111 \rangle$ directions from the vacancy to the four nearest neighbors at the positions $[\bar{1}11]$, $[1\bar{1}1]$, $[11\bar{1}]$, and $[\bar{1}\bar{1}\bar{1}]$, respectively (Fig. 1). The labeling of the defect orientations is formally defined in connection with the \vec{g} tensor (Table II). The last letter of the three-letter orientation label denotes the $\langle 111 \rangle$ axis with

the largest projection onto the direction of g_1 . The first letter denotes the $\langle 111 \rangle$ axis with the second largest projection onto g_1 , and the middle letter the third largest. The defect orientation for the \vec{g} tensor in Table II is thus dba . In Fig. 2 all orientation labels of the angular dependent EPR pattern are indicated.

Watkins also studied motional averaging of the Si-G10 EPR spectrum at temperatures of 30–80 K. At these temperatures only limited reorientation was observed: orientations with labels with the same first two letters flip over, i.e., the reorientation occurs between the two possible choices of the last letter. This observation was confirmed by a stress-induced alignment experiment. Under uniaxial stress some orientations are energetically favored above others. The resulting reorientation also occurs between pairs sharing the first two letters of their label.² These experiments were essential for the construction of a microscopic model. Reorientation at these low temperatures suggests that only an electronic reorientation occurs; in other words, that the positions of the boron atom and the vacancy remain unchanged. This is consistent with experiments on similar centers, such as the phosphorus-vacancy complex.⁸ In that case, the change of the phosphorus-vacancy axis occurs only at room temperature. At those temperatures the boron-vacancy complex anneals already.

The reorientation data show that the defect reorients by a $m_{\{110\}}$ reflection; in our case, between orientations dba and dbc . The plane of reflection is defined by the first two letters: the $db0$, or $(1\bar{1}0)$ plane. The assumption that the reorientation is purely electronic imposes the requirement that both the boron atom and the vacancy be in this plane of reflection. Mainly on these grounds Watkins constructed the atomic model shown in Fig. 1, where the boron atom is on a next-nearest-neighbor position of the vacancy. Given this model, the labeling scheme can be interpreted in terms of the position of the boron atom with respect to the four nearest neighbors of the vacancy. The first letter denotes the silicon neighbor that is also adjacent to the boron atom, the second letter denotes the neighbor that lies in the plane defined by the boron atom, the vacancy, and the first letter atom, while the last letter identifies the neighbor on which most of the unpaired electron is found, i.e., the direction of the Si-1 hyperfine interaction. The reader easily verifies that the orientation of Fig. 1 is dba .

TABLE IV. Reduced hyperfine parameters and calculated LCAO parameters of the silicon hyperfine interactions of the boron-vacancy complex. a , b , and c are in units of kHz. s -character fractions α^2 , p -character fractions β^2 , and localizations η^2 are calculated from the values of a and b , using atomic-orbital data from Ref. 22.

| Tensor | a | b | c | a/b | b/c | α^2 | β^2 | η^2 (%) |
|--------|---------|--------|------|-------|-------|------------|-----------|--------------|
| Si-1 | 297 200 | 48 300 | 1000 | 6.15 | 48.3 | 0.130 | 0.870 | 54.83 |
| Si-2 | 59 747 | 3730 | 784 | 16.02 | 4.76 | 0.281 | 0.719 | 5.12 |
| Si-3 | 56 146 | 3489 | 781 | 16.09 | 4.47 | 0.282 | 0.718 | 4.79 |
| Si-4 | 27 599 | 4263 | 287 | 6.47 | 14.83 | 0.136 | 0.864 | 4.87 |
| Si-5 | 26 403 | 4465 | 255 | 5.91 | 17.49 | 0.126 | 0.874 | 5.04 |
| Si-6 | 25 598 | 3470 | 172 | 7.38 | 20.17 | 0.153 | 0.847 | 4.04 |
| Si-7 | 24 870 | 3419 | 181 | 7.27 | 18.86 | 0.151 | 0.849 | 3.97 |
| Si-8 | 24 046 | 4091 | 171 | 5.88 | 23.89 | 0.125 | 0.875 | 4.61 |

TABLE V. Orientations of the various interactions of the boron-vacancy complex with respect to high-symmetry directions of the lattice. \mathbf{n}_i is the nearest direction for eigenvalue i , ϵ_i is the deviation in degrees. "Shell" is the symmetry shell in the mirror-plane approximation (see text). Data refer to orientation dba .

| Tensor | \mathbf{n}_1 | ϵ_1 | \mathbf{n}_2 | ϵ_2 | \mathbf{n}_3 | ϵ_3 | Shell |
|--------------|---------------------|--------------|----------------|--------------|---------------------|--------------|-------|
| \vec{g} | $[1\bar{1}\bar{1}]$ | 10.5 | $[0\bar{1}1]$ | 8.7 | $[211]$ | 10.5 | |
| B, \vec{A} | $[001]$ | 14.2 | $[1\bar{1}0]$ | 15.9 | $[110]$ | 7.3 | |
| B, \vec{Q} | $[1\bar{1}0]$ | 6.5 | $[11\bar{2}]$ | 13.3 | $[111]$ | 11.8 | |
| Si-1 | $[1\bar{1}\bar{1}]$ | 2.9 | $[0\bar{1}1]$ | 9.4 | $[211]$ | 9.5 | M1 |
| Si-2 | $[1\bar{1}1]$ | 5.6 | $[110]$ | 12.6 | $[1\bar{1}\bar{2}]$ | 13.0 | G1 |
| Si-3 | $[11\bar{1}]$ | 3.7 | $[101]$ | 10.1 | $[1\bar{2}\bar{1}]$ | 10.4 | |
| Si-4 | $[1\bar{1}\bar{1}]$ | 1.0 | $[101]$ | 3.3 | $[12\bar{1}]$ | 3.5 | G2 |
| Si-5 | $[1\bar{1}\bar{1}]$ | 0.8 | $[110]$ | 2.3 | $[1\bar{1}\bar{2}]$ | 2.4 | |
| Si-6 | $[1\bar{1}\bar{1}]$ | 3.5 | $[101]$ | 15.6 | $[12\bar{1}]$ | 15.7 | G3 |
| Si-7 | $[1\bar{1}\bar{1}]$ | 4.9 | $[110]$ | 10.8 | $[1\bar{1}\bar{2}]$ | 11.3 | |
| Si-8 | $[1\bar{1}\bar{1}]$ | 1.7 | $[0\bar{1}1]$ | 0.3 | $[211]$ | 1.5 | M2 |

For a further discussion of this model, the directions of the principal axes of all relevant tensors are given in Table V, as well as angles with respect to the high-symmetry directions of the crystal lattice. We first observe that the \vec{g} tensor deviates only slightly from point-group m symmetry; the near mirror plane is $(0\bar{1}1)$ for orientation dba . The deviation of the pertinent principal axis is only 8.7° . This is consistent with the idea that the electronic structure is mainly determined by the vacancy and its neighbors. The spin density on the boron atom is negligible ($a = 154$ kHz, ^{11}B) compared to that on the silicon atom labeled a ($a = 297$ MHz, Si-1). This near mirror plane is found in all data, except for the boron hyperfine and quadrupole interaction. This is reasonable as just the boron atom breaks the mirror-plane symmetry. In Table V one can verify that hyperfine tensors Si-1 and Si-8 show this near mirror plane (\mathbf{n}_2 nearly parallel to $[0\bar{1}1]$). This means that Si-1 and Si-8 are thought to arise from atoms in the $(0\bar{1}1)$ plane. For Si-1 this is consistent with Watkins's identification of the largest hyperfine interaction with atom a .

In Table V pseudoshells are indicated for the silicon hyperfine interactions. In view of the above observation, Si-1 is called M1 and Si-8 M2. The data in Tables III and IV show that the other six silicon hyperfine tensors occur in pairs. Members of each pair can (approximately) be transformed into each other by the symmetry operation $m_{(0\bar{1}1)}$. This leads us to conclude that these three pairs form pseudo-general-class shells. In the case of pure point-group m symmetry such shells contain two atoms. In Table V these shells are labeled G1, G2, and G3. We conclude that these interactions arise from pairs of atoms lying symmetrically with respect to the (near) mirror plane.

The two tensors from shell G1 have their axial directions along the b and c dangling bonds of the vacancy, the others parallel to the a dangling bond. This leads us to the identification of the tensors of shell G1, (Si-2 and Si-3), with the atom positions c and b . In this way three of the four nearest neighbors of the vacancy are identified. The positions of the other atoms are much less obvious. It is peculiar that all the others have axial directions

parallel to Si-1. Among these eight largest hyperfine interactions, none is found in the d dangling-bond direction. This means that nearly no spin is accommodated in a dangling bond on atom d . About Si-8 one can speculate that it arises from the atom at $[022]$, the first neighbor of the a -atom. In that way, these two atoms form the starting point of a $[011]$ chain along which unpaired spin is transferred in the same way as observed for the vacancy.^{18,19} Because of the low symmetry there is little reason why chains in other directions cannot exist as well. In that case one is tempted to identify the atoms at $[\bar{2}02]$ and $[\bar{2}20]$ with the tensors from G2, Si-4 and Si-5, respectively. They would then be starting points for chains in the $[\bar{1}01]$ and $[\bar{1}10]$ directions. An additional argument for this assignment is the close resemblance of the values of a/b , and hence α^2 and β^2 (Table IV), for the tensors of Si-1, Si-4, Si-5, and Si-8. This is the same argument on which we based the picture of the $[011]$ chain for the vacancy. Chains along the $\langle 011 \rangle$ directions are consistent with theoretically predicted charge disturbances.²³

B. Position of the boron atom: hyperfine interaction

In the preceding section a picture emerged of a defect with a near mirror plane, in which the boron atom plays a minor role in determining the \vec{g} tensor. Here we will focus on the hyperfine interaction with the boron atom itself and evaluate the implications of these hyperfine interactions for the atomic model. According to Watkins's EPR experiments, the boron atom lies in the $db0$, or $(1\bar{1}0)$ plane. Figure 7 shows part of this plane: the atoms on the $[110]$ chain through the vacancy and its neighbors b and d . We will discuss the positions x and x' as candidates for the position of the boron atom.

In the usual interpretation of hyperfine tensors in terms of Fermi-contact and dipole-dipole interaction, as given in Sec. III B, the hyperfine values are proportional to g_N . Hyperfine structure anomaly between ^{10}B and ^{11}B nuclei appears to be absent, as the hyperfine tensors in Table II scale with the g_N values, within experimental error. Therefore, in the discussion to follow, we will limit ourselves to the experimental values of the ^{11}B isotope.

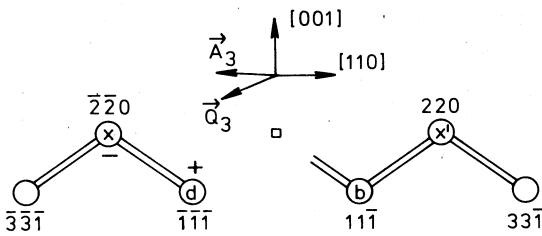


FIG. 7. The $(1\bar{1}0)$ plane of the boron-vacancy complex where, for orientation dba , the boron atom is situated. According to Watkins (Ref. 2), the boron atom is at the position marked x ; the other possibility is x' . The axial direction of the hyperfine (A_3) and quadrupole (Q_3) tensors are indicated.

The axial direction of the hyperfine tensor is the A_3 direction, which deviates only 7.3° from the $[110]$ direction (Table V). When we determine reduced hyperfine parameters as in Sec. III B, we obtain $a = 154.3$ kHz, $b = -345.5$ kHz, and $c = -41.0$ kHz. These different signs of a and b are not consistent with a LCAO picture, if a and b are to be interpreted in terms of atomic orbitals centered on the boron atom itself. Moreover, the anisotropy b is large compared to the isotropic part a , which would lead to abnormally strong p character of $\approx 99\%$.

Because of the very small contact term on the boron atom (154.3 kHz) compared to the first-neighbor silicon atom a (297.2 MHz), one may conclude that at the boron atom the electronic structure is nearly equal to that of the undisturbed silicon lattice. In that case, one should view the BV^0 complex as a B^-V^+ complex, a charge-polarized defect in which boron has trapped an electron, as if it were a normal shallow acceptor. The unbalance in spin between the boron atom and the silicon atom a suggests that at least a substantial part of the anisotropic boron hyperfine tensor must be explained by dipole-dipole interaction between the boron nuclear spin and the electronic spin distribution around the vacancy. We will calculate this interaction for the two possible boron positions x and x' (Figs. 1 and 7).

Position x , the $[\bar{2}\bar{2}0]$ position, was favored by Watkins over the other second neighbor in the $(1\bar{1}0)$ plane, x' at $[220]$. The sign of the stress coupling led him to this choice.² On basis of the hyperfine interaction both positions seem equally probable as the axial direction is close

to $[110]$ and points from the vacancy to these positions. However, when calculating the dipole-dipole interaction between the boron nucleus and the unpaired spin densities around the defect, we have to take into account that these unpaired spin densities are not situated primarily within the vacancy, but in orbitals on the silicon atoms, such as atom a , where 55% of the unpaired spin density is found. One is tempted to do the calculations for atom sites in a $[110]$ direction from the a atom, e.g., the atoms at $[\bar{3}\bar{1}1]$ and $[131]$. These positions, however, are not compatible with the motional experiments because they are not situated in the $db0$ plane. In the preceding section silicon hyperfine interactions Si-1, -2, and -3 were assigned to the three nearest-neighbor lattice sites a , c , and b . The resulting spin distribution, using the values in Table IV, is used for the dipole-dipole calculations. Table VI shows the results for the positions x and x' , if the unpaired spin is assumed to reside in point charges at the atom positions or in Slater-type dangling-bond orbitals.^{18,19} The fit between the experimental and calculated data is not very good. Position x' at $[220]$ seems to be slightly favored by the fact that the axial direction of the calculated tensor is close to the experimental axial direction. We conclude, however, that on these grounds a choice cannot be made.

In Table VI we give also the result of a calculation under the assumption that the total spin density of the three neighbor atoms is concentrated as a point charge in the vacancy, at position $[000]$. Now the fit between the experimental and the calculated tensors is fairly good and the axial direction is $[110]$ (by symmetry), only 7° from the observed direction. Although this assumption is rather unrealistic, these results may be better because Slater-type orbitals underestimate the spatial extent of the spin density, as also indicated by the similarity between the results for point charges and for orbitals in Table VI. The last calculation does not give any clue to the choice between x and x' , because the hyperfine tensors for the two positions are equal by symmetry. Lattice distortions may give a further improvement of this approach. As their magnitudes are rather speculative, such calculations are not given. In the next section we will carry this discussion further in the interpretation of the quadrupole interaction.

Other considerations have to be applied for an explanation of that part of the boron hyperfine interaction that is not given by the dipole-dipole interaction. What remains

TABLE VI. Comparison of calculated hyperfine interactions with experimental values for ^{11}B . "expt" are the experimental values, the sign is reversed with respect to Table II, "PC $[xyz]$ " are the values calculated in point $[xyz]$ for point charges at the positions of the orbitals, "orb $[xyz]$ " are the values calculated for Slater-type orbitals. Given are principal values in kHz; δ is the angle between the axial direction of the experimental tensor and the calculated tensor.

| | B_1 | B_2 | B_3 | δ (deg) | Remarks |
|------------------------------|--------|--------|-------|----------------|------------------------------|
| expt. ^{11}B | -386.5 | -304.5 | 691.0 | | $a = -154.3$ kHz |
| PC $[\bar{2}\bar{2}0]$ | -167.6 | -145.7 | 313.3 | 36 | } Position x |
| orb $[\bar{2}\bar{2}0]$ | -196.1 | -176.3 | 372.4 | 29 | |
| PC $[220]$ | -237.5 | -97.9 | 335.4 | 9 | } Position x' |
| orb $[220]$ | -239.1 | -178.0 | 417.1 | 8 | |
| PC $[\bar{2}\bar{2}0],[220]$ | -289.7 | -289.7 | 579.4 | 7 | $\eta^2 = 64.7\%$ at $[000]$ |

is a small part of the anisotropy and the trace, which has a negative sign with respect to the dipole-dipole part. Here we probably deal with exchange polarization of the paired electrons around the boron atom, through the adjacent unpaired spin. About such effects in silicon quantitative data are hardly known. They have also been discussed for the vacancy.^{18,19}

C. Charge transfer: boron quadrupole interaction

The quadrupole interaction can be described as the interaction between the nuclear quadrupole moment Q and the electric field gradient at the site of the nucleus:

$$Q_{ij} = \frac{eQ}{2I(2I-1)} \frac{\partial^2 V}{\partial x_i \partial x_j}, \quad (11)$$

where e is the electron charge, I is the nuclear spin, and V is the electrostatic potential.^{24,25} Thus, the \vec{Q} tensor is a measure of the total unbalanced charge density around the nucleus, and not only the spin density. It serves, like the hyperfine interaction, as a probe for the electron distribution in the defect, because the unperturbed crystal does not contribute to field gradients. The nuclear quadrupole moments are $8.5 \times 10^{-30} \text{ m}^2$ for ^{10}B and $4.1 \times 10^{-30} \text{ m}^2$ for ^{11}B .²⁰ The measured quadrupole interactions in Table II scale according to these values, so that we may conclude that no measurable anomalies occur, as in the case of the hyperfine interaction. Therefore we will limit ourselves to a discussion of the ^{11}B values.

As quadrupole interactions are caused by unbalanced charges in the defect, we focus on the charge distribution in the boron-vacancy complex. We found that the spin is mainly concentrated on atom a , whereas the d atom carries one net positive charge because it lacks one electron, as inferred from the absence of appreciable hyperfine interaction from the d dangling bond. Thus, in a first approximation, the spin and the charge of the vacancy are located on different atoms. For the a atom this is not completely true: as it has a localization of only 55% spin density, the atom must have a net positive charge of 45% of an electron. The compensating negative charge of 45% is spread out over surrounding silicon atoms. Hyperfine tensors Si-2 to Si-8 account already for 35%. The positive charge on atom d is compensated by a negative charge of the boron atom, where the electronic structure is, to first order, equal to that of the unperturbed silicon crystal. This idea is supported by the absence of hyperfine structure on the boron atom ($a = -154 \text{ kHz}$) that can be related to orbitals located on the boron atom. Figure 7 shows these charges; no spins are indicated as atom a is not situated in this plane. The structural difference between a boron-vacancy complex with a boron at x or x' is only of electronic nature because the atomic structure is the same. However, only for position x can we give a reasonable explanation of the magnitude and direction of the quadrupole tensor.

As in the case of hyperfine tensors we can determine reduced parameters for the quadrupole tensor. We write the principal values as $2q$, $-q+r$, and $-q-r$. q is the quadrupole interaction parameter; r is the deviation from axial symmetry. For our experimental quadrupole split-

ting we have $q = 44.1 \text{ kHz}$ and $r = 18.2 \text{ kHz}$, with an axial direction that deviates 11.3° from the $[111]$ direction. The sign is reversed with respect to Table II because the connected sign of the hyperfine interaction was reversed through the interpretation in the preceding section. The axially is rather poor: $q/r = 2.4$.

As a first approximation we calculate the effect of the positive electronic charge, located on the d atom, at a distance of one bond length from the boron nucleus at x . Such a point charge, at distance r , yields an axially symmetric \vec{Q} tensor, with its axial direction pointing towards the point charge. With Eq. (11) one can evaluate

$$q = \frac{1}{4\pi\epsilon_0} \frac{e^2 Q}{2I(2I-1)} \frac{1}{r^3}. \quad (12)$$

After substitution of the nuclear quadrupole moment we find a quadrupole tensor with $q = 18.3 \text{ kHz}$ and $r = 0 \text{ kHz}$, with its axial direction parallel to $[11\bar{1}]$. This result alone does not explain the experimental values, but if we treat it as a known contribution, we can subtract this tensor (in a Cartesian representation) from the experimental tensor. Then a quadrupole interaction with $q = 47.9 \text{ kHz}$ and $r = 5.7 \text{ kHz}$ remains to be explained. This tensor is more axial ($q/r = 8.4$) than the experimental tensor and its axial direction deviates only 2.5° from the $[111]$ direction.

This resulting axial tensor has to be explained by unbalanced charges at the boron atom itself. It can be related to charge densities arising from partially filled p orbitals in the same way as the hyperfine interaction is related to spin densities. A p orbital gives an axially symmetric quadrupole tensor with

$$q = -\frac{1}{4\pi\epsilon_0} \frac{e^2 Q}{2I(2I-1)} \frac{2}{5} \eta^2 \langle r^{-3} \rangle_p, \quad (13)$$

where η^2 is the fraction of the electronic charge and $\langle r^{-3} \rangle_p$ is the same atomic constant as is used in the analysis of hyperfine interactions. For a boron $2p$ orbital, $\langle r^{-3} \rangle_p = 6.28 \times 10^{30} \text{ m}^{-3}$.²² With a ^{11}B nucleus this will give $q = -600 \text{ kHz}$. In a similar way Watkins analyzed quadrupole interactions of the boron interstitial.¹⁷ This implies that the remaining quadrupole interaction is consistent with 8% of an electronic charge lacking from the symmetric charge distribution associated with tetrahedral symmetry. This means that 8% of the polarized charge is transferred from the boron atom, probably to the silicon atom at d . This effect is not unreasonable as it lowers the Coulombic energy. The reason that we do not observe this transferred charge through the hyperfine interaction on either atom is that equal amounts of spin-up and spin-down density are transferred, as we deal with an electrostatic effect where spins do not play any role.

The lacking charge on the boron atom is 8% of a p orbital pointing in a $[111]$ direction. This is parallel to the unbalanced charge density on the d silicon atom in the missing dangling bond towards the vacancy. This means that the charge disturbance of atom d spreads itself out to

the boron atom in an orbital parallel to its own. This situation strongly resembles the situation which was encountered in the vacancy where also charge is transferred through the $\langle 111 \rangle$ directed bonds, leading to a nearly one-dimensional $\langle 011 \rangle$ -chain defect.^{18,19} For the vacancy this effect is visible on each of the silicon nuclei, because it is paramagnetic charge density. In this case non-paramagnetic charge is transferred, but the mechanism seems to be the same. The experimental observation of this charge transfer is restricted to nuclei having a quadrupole moment, which ²⁹Si has not. Even the order of magnitude of this effect is the same as for the spin transfer, both in the vacancy and in the present defect. Under the earlier assumption that the Si-8 hyperfine tensor originates at [022], there is also a factor of 12 between the spin density on the *a* atom and its neighbor, with parallel axial directions. It is clear that the above interpretation of the quadrupole interaction does not apply to position *x'* for the boron atom.

V. CONCLUSIONS

In this study it has convincingly been shown that ENDOR measurements are a powerful tool for the identification of the microscopic structure of defects. The resolving power of ENDOR is absolutely needed to determine hyperfine and quadrupole parameters that are very small and yet of vital importance because they arise from the impurity constituting the impurity-vacancy pair. Our results for the first time provided proof of the occurrence of boron in the Si-G10 center. Due to the very special nature of the defect, where spin densities are located on other atoms than charge densities, both hyperfine and quadrupole interactions are needed for the construction of the

model. Six of the eight silicon hyperfine tensors are identified with certain lattice positions; some quite firmly (Si-1, Si-2, and Si-3 with the vacancy neighbors *a*, *c*, and *b*), others more tentatively (Si-4, Si-5, and Si-8 with the three neighbor sites of atom *a*).

Our measurements support the original microscopic model with the boron atom at position $[\bar{2}\bar{2}0]$ (*x* in Figs. 1 and 7). From the boron hyperfine interaction we cannot discriminate between *x* and *x'*, but the quadrupole interaction with the boron can only be understood for position *x*. Moreover, the *x'* boron position is not likely to be compatible with the identification of Si-2 and Si-3 hyperfine interactions with the nearest-neighbor positions *c* and *b*, respectively. Because the *x'* position is a nearest neighbor of only *b*, one would expect to see the influence of the boron atom, breaking the symmetry between Si-2 and Si-3 more strongly.

Despite this very detailed information about the defect, a question about its unique low symmetry remains. Why does boron behave differently from all the other substitutional impurities of which a complex with a vacancy has been identified? In all these cases the impurity is at a nearest-neighbor site of the vacancy, resulting in a higher symmetry. From Coulomb-energy arguments one should expect that the boron atom simply changes place with the silicon atom at *d*, cancelling the charge polarization. Perhaps this does not happen because of the small size of the boron atom (a 25% smaller atomic radius than that of silicon). A boron atom at a nearest-neighbor site of the vacancy may cause such a large distortion of the vacancy that it requires an even larger energy than the Coulomb energy of the polarized structure. The recent DLTS experiments on configurational bistability seem to give a clue to this point.

*Present address: Free University Hospital, Postbus 7057, 1007 MB Amsterdam, The Netherlands.

¹E. G. Sieverts, Phys. Status Solidi B 120, 11 (1983).

²G. D. Watkins, Phys. Rev. B 13, 2511 (1976).

³M. Sprenger, R. van Kemp, E. G. Sieverts, and C. A. J. Ammerlaan, J. Electron. Mater. 14A, 815 (1985).

⁴G. D. Watkins, Phys. Rev. 155, 802 (1967).

⁵G. D. Watkins, in *Lattice Defects in Semiconductors 1974*, edited by F. A. Huntley (Institute of Physics, London, 1975), p. 1.

⁶G. D. Watkins (private communication).

⁷G. D. Watkins, Phys. Rev. B 12, 4383 (1975).

⁸G. D. Watkins and J. W. Corbett, Phys. Rev. 134, A1359 (1964).

⁹E. L. Elkin and G. D. Watkins, Phys. Rev. 174, 881 (1968).

¹⁰E. G. Sieverts and C. A. J. Ammerlaan, in *Radiation Effects in Semiconductors 1976*, edited by N. B. Urli and J. W. Corbett (Institute of Physics, London, 1977), p. 213.

¹¹E. G. Sieverts, Ph.D. thesis, University of Amsterdam, 1978.

¹²S. H. Muller, G. M. Tuynman, E. G. Sieverts, and C. A. J. Ammerlaan, Phys. Rev. B 25, 25 (1982).

¹³Yu. V. Gorelkinskii and N. N. Nevinnyi, Phys. Lett. 99A, 117 (1983).

¹⁴A. Chantre, Phys. Rev. B 32, 3687 (1985).

¹⁵S. K. Bains and P. C. Banbury, J. Phys. C 18, L109 (1985).

¹⁶G. D. Watkins, in *Radiation Damage in Semiconductors 1964*, edited by P. Baruch (Dunod, Paris, 1965), p. 97.

¹⁷G. D. Watkins, Phys. Rev. B 12, 5824 (1975).

¹⁸M. Sprenger, Ph.D. thesis, University of Amsterdam, 1986 (copies available through the authors).

¹⁹M. Sprenger, S. H. Muller, E. G. Sieverts, and C. A. J. Ammerlaan, preceding paper, Phys. Rev. B 35, 1566 (1987).

²⁰G. H. Fuller, J. Phys. Chem. Ref. Data 5, 835 (1976).

²¹J. R. Niklas and J. M. Spaeth, Phys. Status Solidi B 101, 221 (1980).

²²J. R. Morton and K. F. Preston, J. Magn. Reson. 30, 577 (1978).

²³E. O. Kane, Phys. Rev. B 31, 5199 (1985).

²⁴T. P. Das and E. L. Hahn, Solid State Phys. Suppl. 1, 1 (1958).

²⁵H. B. G. Casimir, Verh. Teyler's Tweede Genootschap (Nieuwe Reeks) 11, 1 (1936).